New Near-Field and Far-Field Attenuation Models for Free-Space Variable Optical Attenuators

X. M. Zhang, *Student Member, IEEE,* A. Q. Liu, *Member, IEEE,* and C. Lu

***Abstract*—Novel closed-form attenuation models have been developed for free-space variable optical attenuators (VOAs)—one deals with the near-field condition when the two single-mode fibers are aligned very close to each other while the other deals with the far-field condition. In both models, the relationship between mirror (i.e., shutter) position and attenuation is represented by a constant term and another term in the form of an extended error function. The constant term determines the insertion loss, while the error function defines the shape of the attenuation curve. Compared with the conventional model that employs time-consuming numerical integrals, these two models show clearly the physical picture of the attenuation mechanism and provide closed-form expressions of attenuation versus mirror position. They are computationally efficient for attenuator design and optimization. Numerical calculation and experimental study have also been carried out to verify the attenuation models developed in this paper.**

***Index Terms*—Dense wavelength-division multiplexing (DWDM), fiber-optic communication, microelectromechanical systems (MEMS), variable optical attenuator (VOA).**

I. Introduction

VARIABLE optical attenuators (VOAs) are the key components in fiber optical communication systems and have wide applications, such as protecting the sensitive optical receivers, equalizing the power levels of multiple wavelength channels, and flattening the gain of optical amplifiers [1], [2]. Various technologies have been applied to VOAs, such as the Mach–Zehnder interferometer [3], the thin-film filter [4], and the acoustic-wave-induced diffraction [5]. However, attenuators that use shutters/knife edges to block a portion of light in free space have been extensively developed [6]–[10] since they can provide large attenuation range, low insertion loss, and small wavelength/polarization dependence. However, the conventional optomechanical attenuators have slow speed and bulky size, limiting their applications. Microelectromechanical systems (MEMS) technology opens up a new opportunity for free-space attenuators and has shown their competence to provide excellent optical and mechanical performances with additional advantages of high compactness, batch fabrication, and low cost [4], [6]–[9].

The free-space VOAs can be implemented using either the expanded laser beams or the beams directly from the single-mode fibers (SMFs) (i.e., butt coupling). Fig. 1 illustrates the typical configurations. Collimating lenses and quarter-pitch gradient-index (GRIN) lenses are commonly used to expand the light beams, as shown in Fig. 1(a) and (b), respectively. The expanded-beam type has advantages of high attenuation resolution, low insertion loss, and low requirement of mirror position control, making it a good choice for conventional optomechanical VOAs. The butt-coupling type does not need any optical lens; the configuration is simple and compact, as shown in Fig. 1(c). However, the fibers need to be aligned precisely and very near to each other so as to reduce the insertion loss, and the mirror movement should be fine and stable. The MEMS technology meets these requirements. Although various free-space VOAs have been developed, not much effort has been made to address the issue of optical modeling. In free-space VOAs, the attenuation model, which represents the relationship between the attenuation and the mirror (shutter) position, is a key concern for design and optimization. The conventional method is based on the complicated Fresnel–Kirchhoff diffraction integral and mode-overlap integral [10]. It is straightforward but has to involve very time-consuming numerical calculation since the integrals do not have analytical solutions. The influence of the structure parameters on the attenuation cannot be predicted

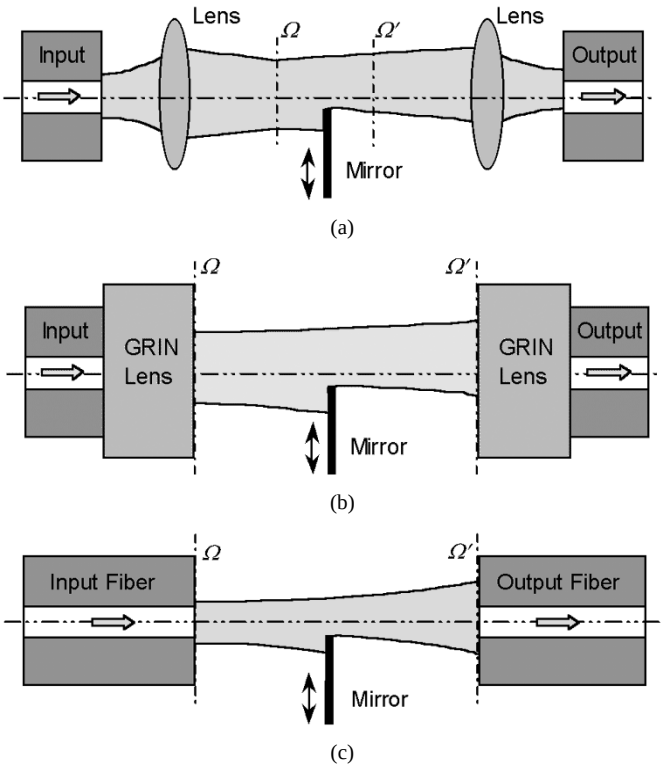

Fig. 1. Typical configurations of the free-space attenuators. (a) Light beam expanded by collimating lenses, (b) by GRIN lenses, and (c) by butt coupling.

Manuscript received September 03, 2003.

The authors are with the School of Electrical and Electronic Engineering, Nanyang Technological University, Singapore 639798 (e-mail: eaqliu@ntu.edu.sg).

Digital Object Identifier 10.1109/JLT.2003.822253

without engaging a large amount of calculations, and any parameter change needs to be recalculated. Besides, the accuracy of the simulation results seriously depends on the grid dimension and the integral areas. If the grid is not fine enough, this method results in error. As an example, when the grid is coarse, the attenuation value tends to approach a certain value (like saturation) in the high attenuation region, as shown in [10, Fig. 7]. However, this prediction is wrong. When the mirror fully blocks the light, the attenuation should be infinity and does not saturate. Therefore, in the conventional method, the fine grid should be used. However, the calculation time increases tremendously. In brief, the conventional method is inconvenient for attenuator design and optimization. The difficulty of the conventional method mainly comes from the fact that it deals with the diffraction and the mode-coupling separately while both are not integrable. If the two integrals are mathematically solved at the same time and also induce some reasonable simplifications, an analytical result may be reached. This paper is motivated by this idea.

The objective of this paper is to develop attenuation models in analytical form for the free-space VOAs. The analytical form inherently enables fast design and improves the physical understanding of the VOAs. In Section II, the conventional attenuation model will be first investigated in detail, and then the far-field model and the near-field model will be derived. The definition of near-field and far-field is determined by comparing the distance from the mirror to the output fiber with the Rayleigh range of the Gaussian beam. If the distance is much smaller than the Rayleigh range, it is near-field; otherwise, it is far-field. The analytical form of the attenuation models represents the physical relationship to guide the attenuator design and also enable faster computation. In Section III, the numerical verification and the experimental results will be discussed. The results predicted by the near-field mode are very close to those given by the conventional model in the near-field condition, while the far-field model gives good agreement with the conventional model in the far-field condition.

II. Attenuation Models

The following three assumptions are used throughout the paper:

1) the scalar optical assumption, i.e., the scalar optical theory is valid;
2) the Gaussian beam assumption, i.e., the light transmitted in a weakly guided SMF can be approximated by Gaussian distribution;
3) the mirror assumption, i.e., the thickness of the mirror is negligible but thick enough to block all the light in the area it covers, the mirror has smooth and straight edge, and it is infinitely large and moves along the η axis from $-\infty$.

The following two assumptions are used in deriving the far-field model and the near-field model, respectively:

4) the far-field assumption (or far-field condition), i.e., the output fiber is far from the mirror plane, more specifically, $z_2 \gg z_R$ (which will be discussed subsequently);
5) the near-field assumption (or near-field condition), i.e., the output fiber is very close to the mirror plane, more specifically, $z_2 \ll z_R$ (which will also be discussed subsequently).

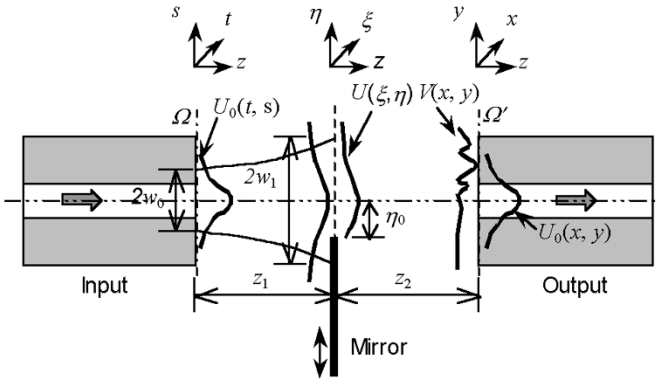

Fig. 2. Diagram for attenuation model of free-space butt-coupling VOA.

Using the Gaussian beam assumption, the light from an SMF is a Gaussian beam with its waist at the fiber facet [11]. In the butt-coupling VOA, the Gaussian beam from the plane Ω is first transmitted to the plane Ω' and then coupled into the output fiber, as shown in Fig. 1(c). Ω and Ω' stand for the positions of the beam waists of the input fiber and the output fiber, respectively. They are right at the facets of the fibers. In the collimated-lens type, the light remains a Gaussian beam after expanded by the lens, but the position of the beam waist changes to the plane Ω. The size and position of the beam waist was studied by Self [12]. Similarly, the lens in the output part also has a corresponding plane Ω'. Only a Gaussian beam in this plane with a certain beam waist can be fully coupled into the output fiber. In the GRIN lenses configuration, the waist of the expanded Gaussian beam is at the GRIN facet [13]. Consequently, by studying the beam propagation and coupling between the planes Ω and Ω', the two expanded-beam configurations follow the same coupling model as the butt-coupling one.

A. Conventional Model

The diagram illustrating the attenuation model of a free-space butt-coupling VOA is shown in Fig. 2. The conventional method uses the light propagation and coupling theories straightforwardly and follows what really happens in the VOA step by step. The light beam from the input SMF propagates to the mirror plane and is partially blocked by the mirror (as a shutter). It is then diffracted to the accepting facet of the output SMF and coupled into the output. In Fig. 2, (s,t,z), (ξ,η,z), and (x,y,z) stand for the coordinate systems in the input fiber facet, the plane after the mirror, and the output fiber facet, respectively. To better explain the models, the plane right after the mirror is named as the mirror plane and the output fiber facet as the facet plane.

The fundamental mode $U_0(t,s)$ of the light beam in the SMFs can be approximated by [11]

$$U_0(t,s) = \sqrt{\frac{2}{\pi w_0^2}} \exp\left\{-\frac{t^2+s^2}{w_0^2}\right\} \tag{1}$$

where w_0 is the waist radius of Gaussian beam. The term $\sqrt{2/\pi w_0^2}$ is used to normalize the light energy to be 1.

After passing through a distance z_1, the light beam reaches the mirror plane and is partially blocked by the mirror, and the field distribution $U(\xi,\eta)$ can be expressed as [11] (2), shown at the bottom of this page, where η_0 is the position of the mirror edge, λ stands for the wavelength, and k, z_R, and w_1 represent the wave number, the Rayleigh range, and the waist radius of Gaussian beam in the mirror plane, respectively, as given by [11]

$$k = \frac{2\pi}{\lambda} \tag{3a}$$

$$z_R = \frac{\pi w_0^2}{\lambda} \tag{3b}$$

$$w_1 = w_0\sqrt{1+\frac{z_1^2}{z_R^2}}. \tag{3c}$$

The light beam is then diffracted to the facet plane. The field distribution $V(x,y)$ can be expressed using the Fresnel–Kirchhoff diffraction formula [14]

$$V(x,y) = \frac{1}{2j\lambda}\iint_{\Sigma} U(\xi,\eta)\frac{\exp\{jkr_{01}\}}{r_{01}}(1+\cos\theta_{01})\,d\xi d\eta \tag{4}$$

where z_2 is the separation between the mirror and the output fiber facet (as shown in Fig. 3), Σ is the integral area, and r_{01} and θ_{01} represent the distance and the angle between the point $A(\xi,\eta)$ in the mirror plane and the point $B(x,y)$ in the output fiber facet given by

$$r_{01} = \sqrt{(x-\xi)^2+(y-\eta)^2+z_2^2} \tag{5}$$

$$\theta_{01} = \arccos\left(\frac{z_2}{r_{01}}\right). \tag{6}$$

The coupling efficiency E_0 represents how much the field distribution $V(x,y)$ is coupled to the fundamental mode $U_0(x,y)$ of the output fiber. It can be obtained by the mode-overlap integral [15]

$$E_0 = \frac{\left|\int\int_{-\infty}^{+\infty} V(x,y)\,U_0^*(x,y)\,dxdy\right|^2}{\int\int_{+\infty}^{-\infty}|V(x,y)|^2\,dxdy\cdot\int\int_{+\infty}^{-\infty}|U_0(x,y)|^2\,dxdy} \tag{7}$$

where $U_0^*(x,y)$ is the conjugate of $U_0(x,y)$, which can be expressed by

$$U_0(x,y) = \sqrt{\frac{2}{\pi w_0^2}}\exp\left\{-\frac{x^2+y^2}{w_0^2}\right\}. \tag{8}$$

$U_0(x,y)$ is the same as (1) except the coordinate system is (x,y) rather than (t,s) since the output fiber is identical to the input fiber. The physical meaning behind this mode-overlap integral is that $V(x,y)$ can be expanded on the bases of a set of orthogonal fiber modes, and (7) expresses the fractional power on the base of $U_0(x,y)$.

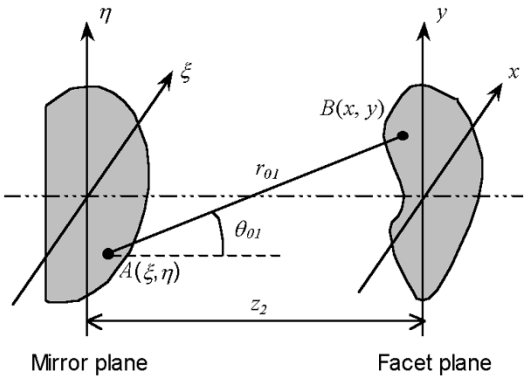

Fig. 3. Diagram of light-beam diffraction from the mirror plane to the facet plane.

The transmission efficiency T_0 from the input fiber to the output fiber is given by

$$T_0 = E_0\frac{\int\int_{+\infty}^{-\infty}|V(x,y)|^2\,dxdy}{\int\int_{+\infty}^{-\infty}|U_0(\xi,\eta)|^2\,d\xi d\eta} = \left|\int\int_{-\infty}^{+\infty} V(x,y)\,U_0^*(x,y)\,dxdy\right|^2. \tag{9}$$

The condition that $U_0(x,y)$ and $U_0(\xi,\eta)$ have unit energy is used. Finally, the attenuation of the VOA is given by

$$L_a = -10\log(T_0). \tag{10}$$

The conventional model expressed in (1)–(10) uses the accurate diffraction formula; thus, it is valid for various optical attenuators. In addition, it can be used to study the field pattern in any position between the two fibers. Fig. 4 illustrates the calculated diffracted patterns at the mirror plane and the facet plane. Fig. 4(a) shows the amplitude and phase distributions in the mirror plane when $z_1 = 10\,\mu$m and $\eta_0 = 0\,\mu$m (i.e., half of the beam is blocked). Within the 15×15-μm^2 observation window, the amplitude pattern has a sudden change across the mirror edge (due to cutoff by the mirror), and most of energy concentrates in a small region. The phase also experiences great changes in the window area (from 20° to −150°). However, it does not vary significantly in the high-amplitude region. Fig. 4(b) and (c) indicates the diffracted patterns in the facet plane when $z_2 = 10\,\mu$m and $z_2 = 500\,\mu$m, respectively. The values of z_2 are intentionally selected to study the near-field pattern and the far-field pattern. In Fig. 4(b), the amplitude has smooth but irregular contours and is also confined in a small region. The phase exhibits rapid change in the direction perpendicular to the mirror edge but slow change in the other direction. This is due to the knife-edge

$$U(\xi,\eta) = \begin{cases} \frac{j2\sqrt{2\pi}w_0}{\lambda\left(2z_1+jkw_0^2\right)}\exp\left\{-jk\left[z_1+\frac{\xi^2+\eta^2}{2z_1\left(1+\frac{z_R^2}{z_1^2}\right)}\right]\right\}\exp\left[-\frac{\xi^2+\eta^2}{w_1^2}\right], & \eta\geq\eta_0 \\ 0, & \eta<\eta_0 \end{cases} \tag{2}$$

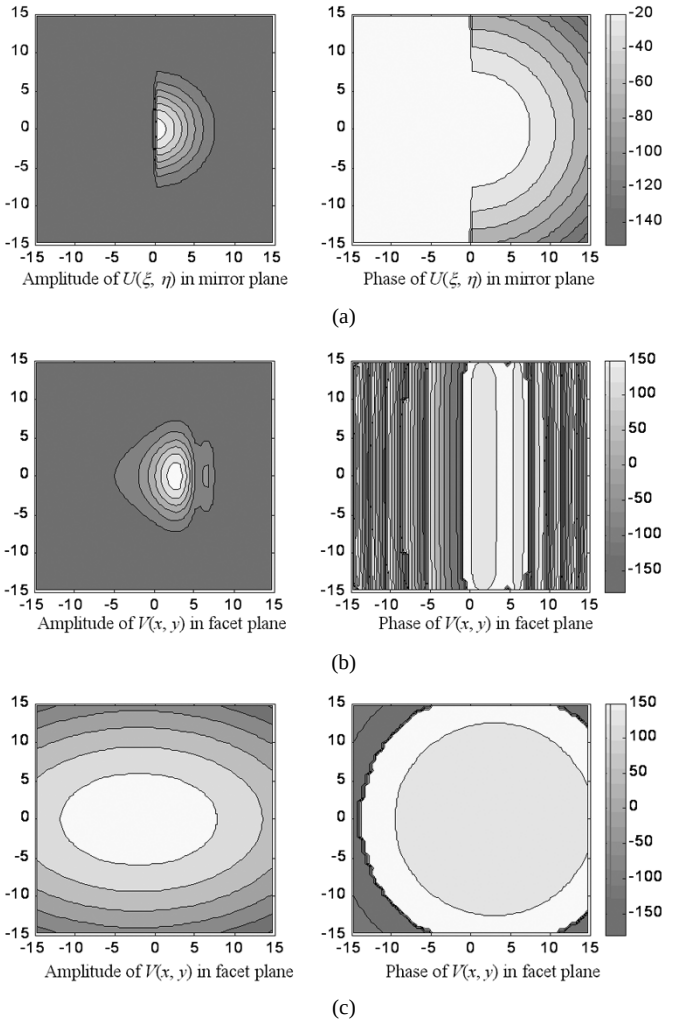

Fig. 4. Amplitude and phase patterns at the mirror plane and the facet planes when half of the input light is blocked ($\eta_0 = 0\ \mu$m): (a) in the mirror plane ($z_1 = 10\ \mu$m); (b) near-field patterns in the facet plane when $z_2 = 10\ \mu$m; and (c) far-field patterns in the facet plane when $z_2 = 500\ \mu$m.

diffraction. In Fig. 4(c), the amplitude and phase distributes smoothly. The amplitude contours appear to be elliptical, while the phase tends to be circular. One interesting point is the change of the pattern centers. In Fig. 4(a), both the amplitude and phase centres are at $\eta = 0\ \mu$m. In Fig. 4(b), they shift nearly identically to about $\eta = 2\ \mu$m. However, in Fig. 4(c), they are separated. The amplitude center moves to about $\eta = -2.5\ \mu$m, while the phase one moves to about $\eta = 4\ \mu$m. These observations suggest that the near-field case is very different from the far-field one, and therefore, different treatments may have to be used in the simplification/analysis. Other parameters in this diffraction pattern study are $\lambda = 1.55\ \mu$m and $w_0 = 5.2\ \mu$m (Corning® SMF-28 SMF [16]).

The conventional method has to employ time-consuming numerical integrals since (4) and (9) are commonly not integrable. Besides, the conventional model cannot show the analytical relationships between the parameters. In the design and optimization of the attenuator, any change of the parameters results in another round of numerical calculation, making it very tedious. Some simplifications should be engaged to obtain a simple analytical result.

B. Far-Field Attenuation Model

Under the far-field assumption, it implies $z_2 \gg w_0$ for common SMFs. Therefore, the diffraction from the mirror plane to the facet plane can be treated as far-field diffraction. As a result, the attenuation model becomes a far-field model for optical attenuator.

The field distribution $U(\xi, \eta)$ in the mirror plane can be simplified as (see Appendix A)

$$U(\xi,\eta) = \begin{cases} \sqrt{\frac{2}{\pi w_1^2}} \exp\left[-a_t\left(\xi^2+\eta^2\right)\right], & \eta \geq \eta_0 \\ 0, & \eta < \eta_0 \end{cases}. \quad (11)$$

Here, the constant phase term is neglected, and a_t is a variable given by

$$a_t = \frac{1}{w_1^2} + \frac{j\pi}{\lambda z_1\left(1+\frac{z_R^2}{z_1^2}\right)}. \quad (12)$$

Under the far-field assumption, $1/r_{01} \approx 1/z_2$ and $\cos\theta_{01} \approx 1$. Substituting into (4), it gives

$$V(x,y) = \frac{1}{j\lambda z_2}\int_{\eta_0}^{+\infty} d\eta \int_{-\infty}^{+\infty} d\xi U(\xi,\eta)\exp\{jkr_{01}\}. \quad (13)$$

Finally, the analytical expression of the transmission efficiency T_0 can be derived. In (9), let Q represent the overlapping integral as expressed by

$$Q = \int\int_{-\infty}^{+\infty} V(x,y)\cdot U_0^*(x,y)\,dxdy. \quad (14)$$

By swapping the integral order and after some mathematical manipulations, Q can be expressed as (see Appendix B)

$$Q = \frac{\pi}{\lambda z_2 w_0 w_1 (a-jb)(c-jd)}\cdot\left[1-\mathrm{EErf}\left(\sqrt{c}\eta_0, -\frac{d}{c}\right)\right] \quad (15)$$

where

$$a = \frac{1}{w_0^2} \quad (16a)$$

$$b = \frac{k}{2z_2} \quad (16b)$$

$$c = \frac{1}{w_1^2} + \frac{ab^2}{a^2+b^2} \quad (16c)$$

$$d = \frac{a^2 b}{a^2+b^2} + \frac{\pi z_1}{\lambda\left(z_R^2+z_1^2\right)} \quad (16d)$$

$$\mathrm{EErf}(p,q) = 2\sqrt{\frac{1+jq}{\pi}}\int_0^p \exp\left\{-(1+jq)t^2\right\}dt \quad (p, q \text{ and } t \text{ are real}). \quad (17)$$

a, b, c, and d are temporary variables. EErf is the extended error function, which simulates the definition of the error function [13]; however, it deals with complex variables, while the error function is limited to real.

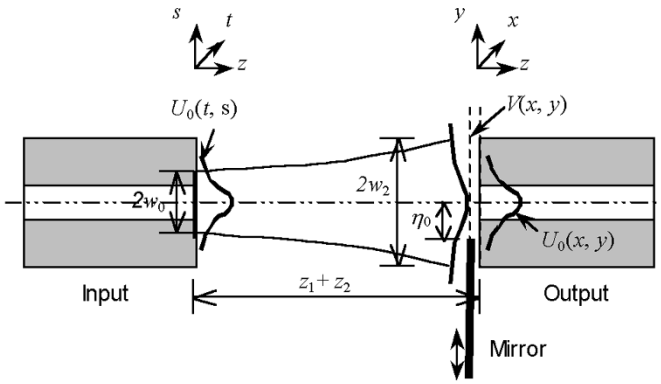

Fig. 5. Attenuation model of the near-field condition.

Substituting (13) and (15) into (9) gives

$$T_0 = |Q|^2 = \frac{A}{4} \cdot \left| 1 - \mathrm{EErf}\left(\sqrt{c}\eta_0, -\frac{d}{c}\right)\right|^2 \tag{18}$$

where

$$A = \frac{4\pi^2}{\lambda^2 z_2^2 w_0^2 w_1^2 (a^2+b^2)(c^2+d^2)}. \tag{19}$$

Finally, the attenuation can be obtained using (10).

It is noted that when z_1 and z_2 are fixed and the mirror moves, the first term in (18) contributes to the attenuation as a constant bias (i.e., insertion loss), whereas the second term defines the shape of the curve. The curve shape is determined by the extended error function. The key features in the mathematical operation of this far-field model are swapping the integral order and expanding r_{01} under the far-field condition. As a result, the integrals become integrable. The analytical result reveals the direct relationship between the mirror position and the attenuation. The attenuation can be estimated without engaging time-consuming numerical integrals.

C. Near-Field Attenuation Model

In most of the MEMS VOAs, the near-field assumption is valid. Under this assumption, it is reasonable to assume that the beam pattern in the facet plane does not vary significantly from that in the mirror plane. Based on this consideration, the diagram of the attenuation model is simplified as shown in Fig. 5. The physical concept is that the mirror is shifted to the facet plane. The light from the input fiber first propagates to the combined mirror plane and facet plane; it is then blocked by the mirror and coupled into the output. In contrast, in the far-field model, the light first propagates to the mirror plane, immediately blocked by the mirror, and then it propagates to the facet plane before being coupled into the output. Viewed from the point of calculation order, the difference is that the light in the far-field model is first blocked and then diffracted, whereas in the near-field one, the order is swapped. From (11), the beam pattern V_{nf} in the facet plane can be simplified as

$$V_{\mathrm{nf}}(x,y) = \begin{cases} \sqrt{\frac{2}{\pi w_2^2}} \exp\left[-\left(\frac{1}{w_2^2} + \frac{j\pi(z_1+z_2)}{\lambda\left[z_R^2+(z_1+z_2)^2\right]}\right)\cdot\left(x^2+y^2\right)\right], & y \geq \eta_0 \\ 0, & y < \eta_0 \end{cases} \tag{20}$$

where w_2 is the waist radius given by

$$w_2 = w_0\sqrt{1+\frac{(z_1+z_2)^2}{z_R^2}}. \tag{21}$$

Then, the transmission efficiency T_{nf} can be derived to be (see Appendix C)

$$T_{\mathrm{nf}} = \frac{B}{4} \cdot \left| 1 - \mathrm{EErf}\left(\sqrt{f}\eta_0, \frac{g}{f}\right)\right|^2 \tag{22}$$

where B, f, and g are variables given by

$$B = \frac{4}{w_0^2 w_2^2 (f^2+g^2)} \tag{22a}$$

$$f = \frac{1}{w_0^2} + \frac{1}{w_2^2} \tag{22b}$$

$$g = \frac{\pi(z_1+z_2)}{\lambda\left[z_R^2+(z_1+z_2)^2\right]}. \tag{22c}$$

Finally, the attenuation can be obtained using (10).

Equation (22) reveals the direct relationship between the attenuation and the mirror position in near-field condition. Similar to that in the far-field model, when the fiber separation (i.e., z_1+z_2) is fixed and the mirror moves, the first term of (22) gives a fixed attenuation, whereas the second term given by the extended error function defines the shape of the curve. The key feature of this model is making the integrals integrable by replacing the knife-edge diffraction with the Gaussian-beam diffraction between the mirror plane and the facet plane.

For a special condition when $z_1 \ll z_R$ and $z_2 \ll z_R$, (22) can be further simplified to be (see Appendix C)

$$T_{\mathrm{nf}} = \frac{1}{4}\left[1 - \mathrm{Erf}\left(\frac{\sqrt{2}\eta_0}{w_0}\right)\right]^2. \tag{23}$$

This equation is valid only under conditions given previously here and may have very limited applications.

III. Discussions and Experiment

A. VOA With Tilting Mirror

The diagrams of the attenuation models in Figs. 2 and 5 assume implicitly that the mirror moves perpendicularly to the optical axis between the two fibers. However, the mirror can also be configured to tilt at a certain angle, as shown Fig. 6. In this way, the back reflection can be greatly reduced if the angle is properly chosen (8 or 12°) [7], [18]. The near-field model can be used directly since the fiber separation does not change with the mirror position. In the far-field case, the far-field model can be used by varying z_1 and z_2 with the position of the mirror as expressed by

$$z_1 = z_{10} - \eta_0 \tan\varphi \tag{24}$$

$$z_2 = z_{20} + \eta_0 \tan\varphi \tag{25}$$

where φ stands for the tilting angle, and z_{10} and z_{20} denote the distances from the mirror to the input and the output fiber, respectively, when the mirror moves to the optical axis. It is noted that η_0 is negative when the mirror is below the optical axis.

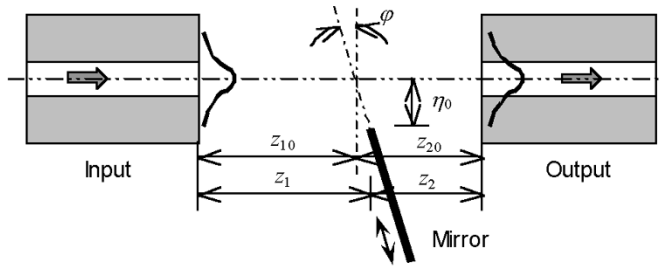

Fig. 6. VOA using a tilting mirror.

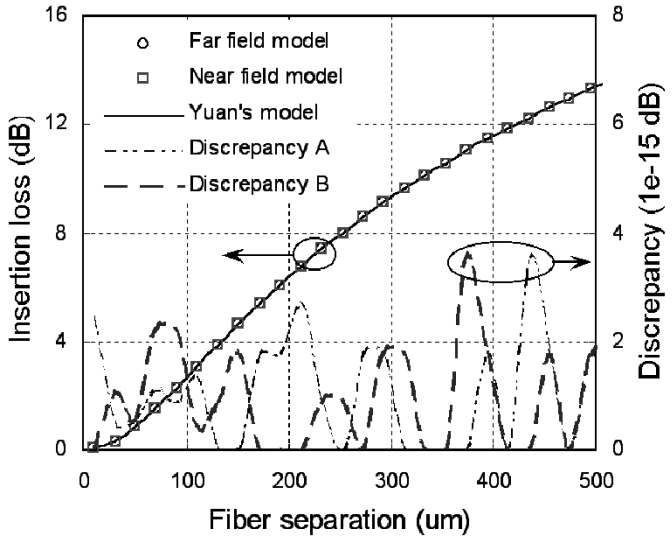

Fig. 7. Comparison of the insertion loss given by different attenuation models. Discrepancy A and B represent the differences of the far-field model with Yuan's model and the near-field model with Yuan's model, respectively.

B. Numerical Analysis

To verify the validity of the far-field and the near-field model, the insertion losses predicted by the models are first examined. When $\eta_0 = -\infty$, that is, the mirror is fully out of the light path, the attenuation between the two fibers represents the insertion loss. According to (18) and (22), insertion losses predicted by the far-field and the near-field model $\mathrm{IL_{ff}}$ and $\mathrm{IL_{nf}}$ are given by

$$\mathrm{IL_{ff}} = -10\log\left[\frac{4\pi^2}{\lambda^2 z_2^2 w_0^2 w_1^2 (a^2+b^2)(c^2+d^2)}\right] \quad (26)$$

$$\mathrm{IL_{nf}} = -10\log\left[\frac{4}{w_0^2 w_2^2 (f^2+g^2)}\right]. \quad (27)$$

The variables a, b, c, d, f, and g are as defined in (16a)–(16d), (22b), and (22c).

A widely used insertion-loss model was developed by Yuan *et al.* in [13]. If only the fiber separation is considered, the insertion loss can be expressed as

$$\mathrm{IL_y} = -10\log\left[\frac{4z_R^2}{4z_R^2 + (z_1+z_2)^2}\right]. \quad (28)$$

The comparison is shown in Fig. 7. When the fiber separation changes from 5 to 500 μm, the attenuation gradually increases from 0.03 to 13.5 dB. The curves of the models are very close. Discrepancy A shows the difference between the far-field model and Yuan's model, while Discrepancy B shows the difference between the near-field model and Yuan's model. The maximum discrepancy of insertion loss is smaller than 4×10^{-15} dB. Therefore, the far-field and the near-field model predict the insertion losses very accurately.

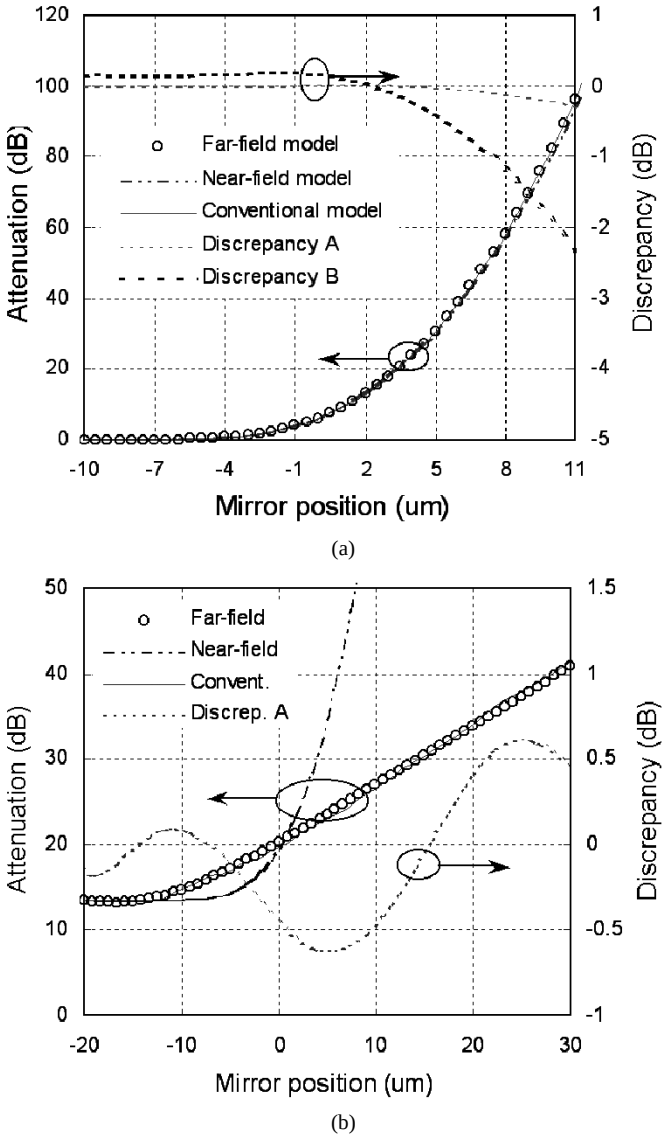

Fig. 8. Comparison of the attenuation models. (a) $z_1 = z_1 = 10$ μm (near-field condition); (b) $z_1 = z_1 = 500$ μm (far-field condition). Discrepancy A and Discrep. A represent the differences of the far-field model with Yuan's model, and Discrepancy B shows the difference of the near-field model with Yuan's model.

Then, the attenuation models are compared with the conventional model in the cases of $z_1 = z_2 = 10$ μm and $z_1 = z_2 = 500$ μm, as shown in Fig. 8(a) and (b), respectively. The input and output fibers are identical, both use Corning SMF-28 SMF ($w_0 = 5.2$ μm and $z_R = 54.8$ μm). Therefore, it satisfies the near-field condition for $z_1 = z_2 = 10$ μm and the far-field condition for $z_1 = z_2 = 500$ μm. In the near-field case, as show in Fig. 8(a), the attenuation varies from about 0.14 to 95 dB when the mirror moves from -10 to 11 μm. The three models overlap each other. Discrepancy A shows the difference between the far-field model and the conventional model, and Discrepancy B shows the difference between the near-field and the conventional model. The near-field model is nearly identical

to the conventional model, especially when the mirror position is less than 5 μm. The maximum difference is -0.28 dB (-0.3%) when the mirror position is at 11 μm. In contrast, the far-field model predicts higher attenuation in the low attenuation level (0.14–dB deviation) and considerably lower value in the high attenuation range (maximum deviation -2.3 dB). Therefore, the near-field model is valid in the near-field condition.

In the far-field case, as show in Fig. 8(b), the near-field differs from the conventional model significantly, while the far-field model does marginally. The attenuation given by the far-field model changes from 13.5 to 41.4 dB when the mirror moves from -20 to 30 μm. Discrep. A represents the difference between the far-field model and the conventional model. The deviation ranges within -0.62 (-2%) to $+0.61$ dB ($+2\%$). Therefore, the far-field model is suitable for the far-field condition.

It is also observed in Fig. 8 that the attenuator has small insertion loss and high attenuation range if the fibers are aligned very close to each other (near-field configuration), but the attenuation curve is very nonlinear. On the contrary, the attenuator of the far-field configuration has a linear attenuation curve but a high insertion loss and small attenuation range. A good design for attenuators should compromise between them.

The far-field and near-field models have great advantages over the conventional model in term of computational speed. As an example, the conventional model takes a computer time of 2.3 h to calculate the attenuation value corresponding to one mirror position. It is very tedious to obtain the entire curve of attenuation versus mirror positions. In contrast, the far-field model needs 2-ms computer time, while the near-field model requires only 0.4-ms computer time. A grid of 0.25 μm and an integral area of 30×30 μm are used for the conventional model. Computer and software are the same when comparing the speed of the three models.

C. Experimental Verification

To verify the attenuation model, a MEMS VOA has been developed, as shown in Fig. 9. Two SMFs are aligned very close to each other, one as input fiber and the other as output fiber. A mirror is inserted into the light path between the two fibers as a shutter to block a portion of the light. To obtain variable attenuation, a proprietary drawbridge actuator [6], [19] is employed. The mirror located at the end of a L-shaped plate is mounted vertically on a mounting plate by a side holder. The mounting plate is hung over the substrate by a triangular drawbridge structure. Three thin bending beams are used to connect the mounting plate to the holding plate. When a potential difference is applied between the mounting plate and the electrode (on the substrate), the bending beams deform, and thus, the mirror moves down.

The MEMS VOA is fabricated using the silicon surface micromachining technology. The close-up of the mirror and the input fiber is shown in Fig. 10. The fibers are aligned using translation stages and then fixed to the substrate through the use of a strong adhesive. The distances between the fiber terminals and the mirror are both about 10 μm. The flat mirror has a size of 40×40 μm and is formed by coating a 0.5-μm-thick gold layer on a 1.5-μm-thick polysilicon layer. The gold layer helps to fully block the light since the polysilicon layer is nearly transparent to the infrared light. The lower edge of the mirror is designed to be 66 μm high over the substrate, which allows most of the light to pass through when no voltage is applied.

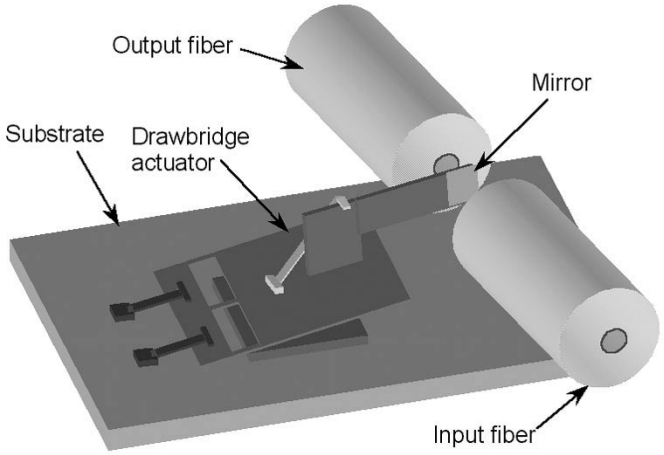

Fig. 9. Schematic of the MEMS VOA using drawbridge actuator.

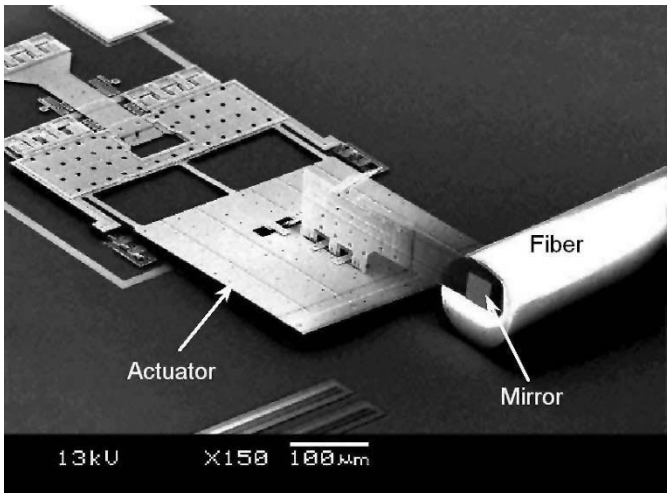

Fig. 10. Scanning electron microscope (SEM) micrograph of the MEMS VOA.

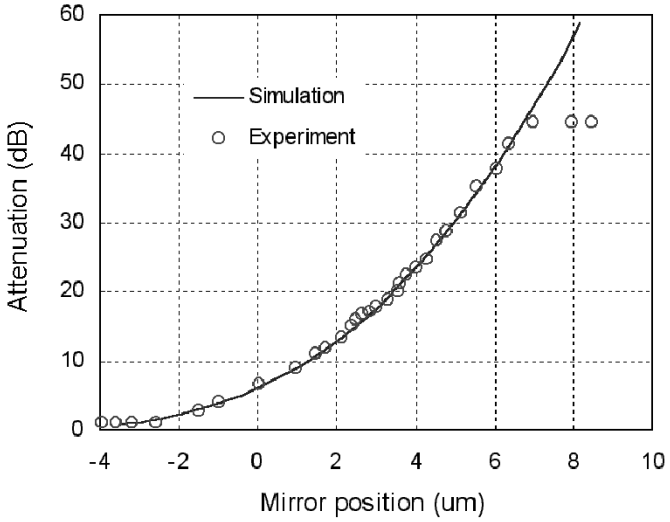

Fig. 11. Comparison of the experiment with the near-field model.

The measurement data is compared with the near-field model, as shown in Fig. 11. The VOA has an insertion loss of 1.5 dB at a

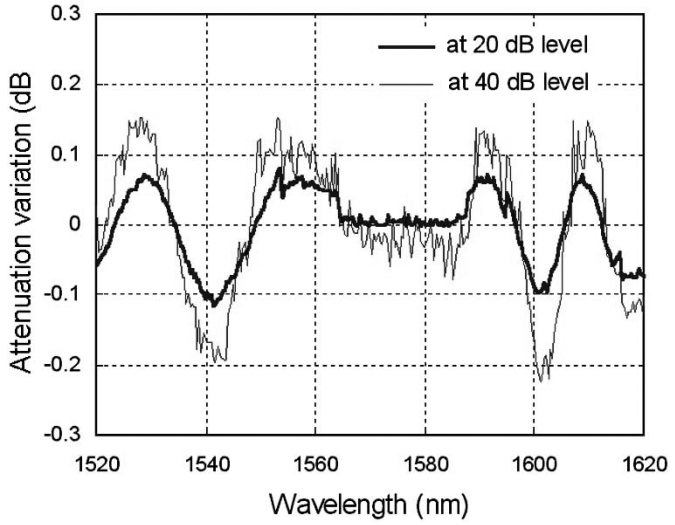

Fig. 12. Wavelength dependence of the VOA at different attenuation levels.

1.55-μm wavelength when no voltage is applied. This insertion loss is mainly introduced by three sources: 1.0 dB from the angular/lateral misalignment between the input and output fibers that are fixed to the substrate by the adhesive; 0.4 dB from the Fresnel reflection of air/glass interfaces in the fiber ends; and 0.1 dB from the fiber separation. To make the simulation comparable to the experiment, an insertion loss of 1.4 dB is added to the simulation data. When the mirror is actuated to move in the light path, the attenuation continuously increases to its maximum value of 45 dB when the mirror moves to about -7 μm. Further movement of the mirror does not produce higher attenuation as predicted by the near-field model since the signal power becomes too weak in our experimental setup and has reached the detector noise floor. In Fig. 11, the simulation result using the near field model is very close to the experimental result over the attenuation range.

The wavelength dependence of the VOA is shown in Fig. 12. In the measurement, the VOA is first set at a certain attenuation level, and then a tunable laser source (ANDO AQ4321) is used to sweep the input wavelength from 1520 to 1620 nm. Fig. 12 illustrates the attenuation fluctuations when the VOA is set at 20 and 40 dB, respectively. Both curves are irregular and have the same trend. However, the curve of the 40 dB is not as smooth as that of the 20 dB, probably due to the noise. In Fig. 12, the peak-to-peak variation is measured to be about 0.20 dB at the 20-dB level and 0.38 dB at the 40-dB level. The VOA also has the variations of 0.17 and 0.35 dB at the attenuation levels of 10 and 30 dB, respectively (not shown in Fig. 12). The wavelength dependence variation tends to increase with the increase of the attenuation level, but the value is small. In this sense, the VOA is not seriously wavelength dependent.

IV. Conclusion

Analytical attenuation models are developed for free-space optical attenuators with near-field and far-field configurations. Numerical and experimental studies show that the near-field and the far-field model are accurate in their specific conditions. The near-field model is especially useful for MEMS VOAs since most of the designs use very small fiber separation so as to reduce the insertion loss. Although the attenuation models are studied for the attenuators using butt-coupling fibers, they apply equally well to the attenuators using collimating lenses and GRIN lenses. In addition, they are useful for studying the transient state of optical switches and optical cross-connects, i.e., the change of optical signals when one channel is switched ON/OFF. The attenuation models are developed based on the scalar optics; the influence of the polarization and the precise shape of mirror edge, which may not be negligible at very high attenuation levels, needs further study.

Appendix A
Simplification of Light Beam in the Mirror Plane

When $\eta \geq \eta_0$, by using the relationships that $z_R = \pi w_0^2/\lambda$, $k = 2\pi/\lambda$, and $w_1 = w_0\sqrt{1+z_1^2/z_R^2}$, (2) can be further derived to be

$$\begin{aligned} U(\xi,\eta) &= \frac{j2\sqrt{2\pi}w_0}{\lambda(2z_1+jkw_0^2)} \\ &\quad \cdot \exp\left\{-jk\left[z_1+\frac{\xi^2+\eta^2}{2z_1\left(1+\frac{z_R^2}{z_1^2}\right)}\right]\right\}\exp\left[\frac{\xi^2+\eta^2}{w_1^2}\right] \\ &= \frac{j\sqrt{2\pi}w_0}{\lambda(z_1+jz_R)}\exp\left[-jkz_1-a_t\left(\xi^2+\eta^2\right)\right] \\ &= \sqrt{\frac{2}{\pi w_1^2}}\exp\left\{-j\left(kz_1-\phi_t\right)\right\}\exp\left[-a_t\left(\xi^2+\eta^2\right)\right] \end{aligned} \tag{A1}$$

where

$$a_t = \frac{1}{w_1^2}+\frac{j\pi}{\lambda z_1\left(1+\frac{z_R^2}{z_1^2}\right)} \tag{A2}$$

and ϕ_t is an phase term given by

$$\phi_t = \arctan\left(\frac{z_1}{z_R}\right). \tag{A3}$$

Ignore the constant phase term in (A1), and then

$$U(\xi,\eta) = \sqrt{\frac{2}{\pi w_1^2}}\exp\left[-a_t\left(\xi^2+\eta^2\right)\right]. \tag{A4}$$

Appendix B
Simplification of Overlapping Integral in the Far-Field Model

The term r_{01} needs to be expanded to the polynomial of x, y, ξ, and η. Otherwise, (13) is not integrable. In the mirror plane, most of the light energy of the Gaussian beam is emitted from a limited area. Similarly, in the facet plane of the output fiber, only the light passing through the limited area around the core contributes to the output. For example, if the interested area in the mirror plane is a circle with radii of $5w_1$, the light energy out of this area is only about 10^{-21} of the total energy. From this point of view, the attenuator has small apertures, and therefore, the

beam propagation can be treated as a Fresnel diffraction [11]. r_{01} is approximated to the first order as

$$r_{01} = \left[z_2^2 + (x-\xi)^2 + (y-\eta)^2\right]^{1/2} \approx z_2 + \frac{1}{2z_2}\left[(x-\xi)^2 + (y-\eta)^2\right]. \quad \text{(A5)}$$

Substituting (11) and (13) into (14) and swapping the integral order obtains

$$\begin{aligned} Q &= \frac{1}{j\lambda z_2}\int_{-\infty}^{+\infty} dx \int_{-\infty}^{+\infty} dy\, U_0^*(x,y) \\ &\quad \cdot \int_{-\infty}^{+\infty} d\xi \int_{\eta_0}^{+\infty} d\eta\, U(\xi,\eta)\exp\{jkr_{01}\} \\ &= \frac{1}{j\lambda z_2}\int_{-\infty}^{+\infty} d\xi \int_{\eta_0}^{+\infty} d\eta\, U(\xi,\eta) \\ &\quad \cdot \left[\int_{-\infty}^{+\infty} dx \int_{-\infty}^{+\infty} dy\, U_0^*(x,y)\exp\{jkr_{01}\}\right]. \end{aligned} \quad \text{(A6)}$$

Let

$$\begin{aligned} S &= \int_{-\infty}^{+\infty} dx \int_{-\infty}^{+\infty} dy\, U_0^*(x,y)\exp\{jkr_{01}\} \\ &= \sqrt{\frac{2}{\pi w_0^2}}\exp\{jkz_2\}\cdot \int_{-\infty}^{+\infty} dx \int_{-\infty}^{+\infty} dy \\ &\quad \cdot \exp\left\{-\frac{x^2+y^2}{w_0^2} + \frac{jk}{2z_2}\left[(x-\xi)^2 + (y-\eta)^2\right]\right\} \\ &= \frac{\sqrt{2\pi}}{w_0(a-jb)}\exp\{jkz_2\}\cdot\exp\left\{-\frac{ab}{b+ja}\left(\xi^2+\eta^2\right)\right\} \end{aligned} \quad \text{(A7)}$$

where a and b are temporary variables given by

$$a = \frac{1}{w_0^2} \quad \text{(A8)}$$

$$b = \frac{k}{2z_2}. \quad \text{(A9)}$$

Neglecting the constant phase term and then substituting (11) and (A7) into (A6) reaches

$$\begin{aligned} Q &= \frac{2}{\lambda z_2 w_0 w_1 (a-jb)}\int_{-\infty}^{+\infty} d\xi \int_{\eta_0}^{+\infty} d\eta \\ &\quad \cdot \exp\left\{-\left(a_t + \frac{ab}{b+ja}\right)\left(\xi^2+\eta^2\right)\right\} \\ &= \frac{\pi}{\lambda z_2 w_0 w_1 (a-jb)(c-jd)}\left[1 - \mathrm{EErf}\left(\sqrt{c}\eta_0, -\frac{d}{c}\right)\right] \end{aligned} \quad \text{(A10)}$$

where

$$c = \frac{1}{w_1^2} + \frac{ab^2}{a^2+b^2} \quad \text{(A11)}$$

$$d = \frac{a^2 b}{a^2+b^2} + \frac{\pi}{\lambda z_1\left(1+\frac{z_R^2}{z_1^2}\right)} \quad \text{(A12)}$$

and EErf is the extended error function defined by

$$\mathrm{EErf}(x,t) = \frac{2}{\sqrt{\pi}}\int_0^x \exp\left\{-(1+jt)\eta^2\right\} d\left(\sqrt{1+jt}\eta\right) \quad (x \text{ and } t \text{ are real}). \quad \text{(A13)}$$

The extended error function simulates the definition of the error function so as to deal with the complex whereas the error function is limited to the real.

Appendix C
Transmission Efficiency of the Near-Field Model

From (9), the transmission efficiency T_{nf} can be expressed as

$$\begin{aligned} T_{\mathrm{nf}} &= \left|\int_{+\infty}^{-\infty}\int V_{\mathrm{nf}}(x,y)\, U_0^*(x,y)\, dxdy\right|^2 \\ &= \left|\int_{-\infty}^{+\infty} dx \int_{\eta_0}^{+\infty} dy \sqrt{\frac{2}{\pi w_2^2}}\right. \\ &\quad \cdot \exp\left\{-\left(\frac{1}{w_2^2} + \frac{j\pi(z_1+z_2)}{\lambda\left[z_R^2 + (z_1+z_2)^2\right]}\right)\left(x^2+y^2\right)\right\} \\ &\quad \left.\cdot \sqrt{\frac{2}{\pi w_0^2}}\exp\left\{-\frac{x^2+y^2}{w_0^2}\right\}\right|^2 \\ &= \frac{4}{\pi^2 w_0^2 w_2^2}\left|\int_{\eta_0}^{+\infty} dy \int_{-\infty}^{+\infty} dx \exp\left\{-(f+jg)\left(x^2+y^2\right)\right\}\right|^2 \\ &= \frac{1}{w_0^2 w_2^2 (f^2+g^2)}\cdot\left|1 - \mathrm{EErf}\left(\sqrt{f}\eta_0, \frac{g}{f}\right)\right|^2 \end{aligned} \quad \text{(A14)}$$

where f and g are intermediate variables representing

$$f = \frac{1}{w_0^2} + \frac{1}{w_2^2} \quad \text{(A15)}$$

$$g = \frac{\pi(z_1+z_2)}{\lambda\left[z_R^2 + (z_1+z_2)^2\right]}. \quad \text{(A16)}$$

In case of $z_1 \ll z_R$ and $z_2 \ll z_R$, it is reasonable to let $w_2 \approx w_0$. As a result, $f \approx 2/w_0^2$ and

$$g \approx \frac{\pi(z_1+z_2)}{\lambda z_R^2} \approx \frac{z_1+z_2}{2z_R}\cdot\frac{2}{w_0^2} \ll f.$$

Equation (A14) can be further simplified to be

$$T_{\mathrm{nf}} = \frac{1}{4}\left|1 - \mathrm{EErf}\left(\frac{\sqrt{2}\eta_0}{w_0}, 0\right)\right|^2 = \frac{1}{4}\left|1 - \mathrm{Erf}\left(\frac{\sqrt{2}\eta_0}{w_0}\right)\right|^2. \quad \text{(A17)}$$

References

[1] N. Cockroft, "Array-based VOA's offer compact signal control," *WDM Solutions*, vol. 3, no. 6, pp. 81–86, 2001.

[2] S. Cohen, "Novel VOAs provide more speed and utility," *Laser Focus World*, vol. 36, no. 11, pp. 139–146, 2000.

[3] K. Kawai, M. koga, M. Okuna, and T. Kitoh, "PLC type compact variable optical attenuator for photonic transport network," *Electron. Lett.*, vol. 34, no. 3, pp. 264–265.
[4] J. E. Ford, J. A. Walker, D. S. Greywall, and K. W. Goossen, "Micromechanical fiber-optic attenuator with 3 μs response," *J. Lightwave Technol.*, vol. 16, pp. 1663–1670, Sept. 1998.
[5] N. A. Riza and Z. Yaqoob, "Submicrosecond speed variable optical attenuator using acoutooptics," *IEEE Photon. Technol. Lett.*, vol. 13, pp. 693–695, July 2001.
[6] X. M. Zhang, A. Q. Liu, C. Lu, and D. Y. Tang, "MEMS variable optical attenuator using low driving voltage for DWDM systems," *IEE Electron. Lett.*, vol. 38, no. 8, pp. 382–383, 2002.
[7] C. Marxer, P. Griss, and N. F. de Rooij, "A variable optical attenuator based on silicon micromechanics," *IEEE Photon. Technol. Lett.*, vol. 11, pp. 233–235, Feb. 1999.
[8] B. Barber, C. R. Giles, V. Askyuk, R. Ruel, L. Stulz, and D. Bishop, "A fiber connectorized MEMS variable optical attenuator," *IEEE Photon. Technol. Lett.*, vol. 10, pp. 1262–1264, Sept. 1998.
[9] S. S. Yun, Y. Y. Kim, H. N. Kown, W. H. Kim, J. H. Lee, Y. G. Lee, and S. C. Jung, "Optical characteristics of a micromachined VOA using successive partial transmission in a silicon optical leaker," in *Proc. Optical MEMs 2002*, Lugano, Switzerland, Aug. 2002, pp. 51–52.
[10] C. R. Giles, V. Aksyuk, B. Barber, R. Ruel, L. Stulz, and D. Bishop, "A silicon MEMS optical switch attenuator and its use in lightwave subsystems," *IEEE J. Select. Topics Quantum Electron.*, vol. 5, pp. 18–25, Jan.–Feb. 1999.
[11] A. K. Ghatak and K. Thyagarajan, *Optical Electronics*. Cambridge, U.K.: Combridge Univ. Press, 1989, p. 141, 142, and 410.
[12] S. A. Self, "Focusing of spherical Gaussian beams," *Appl. Opt.*, vol. 22, no. 5, pp. 658–661, 1983.
[13] S. Yuan and N. A. Riza, "General formula for coupling-loss characterization of single-mode fiber collimators by use of gradient-index rod lenses," *Appl. Opt.*, vol. 38, no. 15, pp. 3214–3222, 1999.
[14] M. Born and E. Wolf, *Principles of Optics: Electromagnetic Theory of Propagation, Interference and Diffraction of Light*, 6th ed. Cambridge, U.K.: Cambridge Univ. Press, 1997, pp. 378–382.
[15] H. Kogelnik, "Coupling and conversion coefficients for optical modes," in *Proc. Symp. Quasi-Optics*, New York, June 8–10, 1964, pp. 333–347.
[16] *Corning® SMF-28™ Optical Fiber Product Information*, Corning Inc., 2001, pp. 1–4.
[17] S. Martinez and B. Courtois, "Insertion loss in micromachined free-space optical cross-connects due to fiber misalignments," in *Proc. SPIE 4408*, 2001, pp. 289–300.
[18] M. Takahashi, "Variable light attenuator of improved air-gap type with extremely low returning light," in *Proc. ITMC '94*, Hamamatsu, Japan, May 10–12, 1994, pp. 947–950.
[19] A. Q. Liu, X. M. Zhang, V. M. Murukeshan, Q. X. Zhang, Q. B. Zou, and S. Uppili, "An optical crossconnect (OXC) using drawbridge micromirrors," *Sens. Actuators A, Phys.*, vol. 97–98, pp. 227–238, 2002.

X. M. Zhang (S'03) received the B.Eng. degree in precision mechanical engineering from the University of Science & Technology of China, Hefei, Anhui Province, in 1994 and the M.Eng. degree in optical instrumentation from the Shanghai Institute of Optics & Fine Mechanics, the Chinese Academy of Science, Jiading, Shanghai, in 1997. Since then, he has been working toward the Ph.D. degree in microelectromechanical systems (MEMS) at the Department of Mechanical Engineering, National University of Singapore.

Currently, he is a Research Associate at the School of Electrical & Electronic Engineering, Nanyang Technological University, Singapore. His research interests include optical MEMS, optical communication, and photonics.

A. Q. Liu (M'03) received the M.S.E. degree in applied physics and the B.Eng. degree in mechanical engineering from Xi'an Jiaotong University, Xi'an, China, in 1988 and 1982, respectively, and the Ph.D. degree from the National University of Singapore (NUS) in 1994.

He worked in the DSO National Laboratory in 1995 and then joined the Institute of Materials Research & Engineering (IMRE) as a Senior Research Fellow in 1997. Currently, he is an Associate Professor with the Division of Microelectronics, School of Electrical & Electronic Engineering, Nanyang Technological University (NTU), Singapore. His research interests are in MEMS technology in infocom applications and MEMS design, fabrication, and integration.

C. Lu received the B.Eng. degree from Tsing Hua University, Beijing, China, in 1985 and the M.Sc. and Ph.D. degrees from the University of Manchester Institute of Science and Technology (UMISI), Manchester, U.K., in 1987 and 1990, respectively.

He joined the School of Electrical and Electronic Engineering, Nanyang Technological University, Singapore, in 1991, where he is currently an Associate Professor in the Communication Division. His research interests are in the area of fiber-optic components and optical communication systems and networks.